ISSN 1027-4510, Journal of Surface Investigation. X-ray, Synchrotron and Neutron Techniques, 2015, Vol. 9, No. 5, pp. 1044–1055. © Pleiades Publishing, Ltd., 2015.

Structure Phases of Fe Nanoparticles in Vertically Aligned Multi-Walled Carbon Nanotubes[1]

N. G. Chechenin[a], P. N. Chernykh[a], E. A. Vorobyeva[a], M. V. Dutka[b], D. I. Vainshtein[b], and J. Th. M. De Hosson[b]

[a] *Skobeltsyn Institute of Nuclear Physics, Moscow State University, Moscow, 119991 Russia*

[b] *Department of Applied Physics, Materials Innovation Institute, University of Groningen, Nijenborgh 4, 9747 AG Groningen, The Netherlands*

e-mail: chechenin@sinp.msu.ru

Received March 16, 2015

Abstract—Structure and composition of arrays of vertically aligned multi-walled carbon nanotubes grown by continuous injection chemical vapor deposition method were studied using the high resolution transmission electron microscopy combined with energy dispersion spectrometry. A portion of injected Fe catalyst was found in the form of nanosized single crystalline particles with a variety of the structures of α-Fe(C), γ-Fe(C) and orthorhombic Fe_3C phases encapsulated in the carbon nanotube channel or incorporated into the carbon nanotube wall. A thorough analysis revealed not only the lattice expansion of the γ-Fe(C) phase due to incorporation of carbon atoms but also a monoclinic distortion of the cubic lattice with orts $c > a = b$ and square base transformed into a rhombic one. The monoclinic lattice distortion was referred to the uniaxial symmetry of the encapsulating tube. No evident coherency was observed in the atomic arrangement at the interface between Fe particle and inner shell of the carbon tube, as well as in the atomic arrangement of neighboring graphene shells of the carbon nanotube wall, meaning that the chirality of the shells is not coherent.

Keywords: multi-walled carbon nanotubes, ferrocene, nanocrystalline gamma-iron, high resolution transmission electron microscopy, chirality

DOI: 10.1134/S1027451015050237

INTRODUCTION

The outstanding properties of carbon nanotubes (CNTs) as a functional material can be demonstrated in full when CNTs are aligned (ACNTs) along a certain direction. As a consequence, growth methods of ACNTs are hot topics since early time of CNT production [1]. Chemical vapor deposition (CVD) on an oxidized nanoporous silicon [2], on nanoislands of Fe obtained by a post treatment of Fe-implanted SiO_2 film [3], microwave [4–6] or direct current [7, 8] plasma enhanced chemical vapor deposition (PECVD) in a particular carbonaceous atmosphere are used. A common feature of the growth methods is the predepositing of the catalyst shell (Ni, Co or other transition elements) of certain thickness on the substrate. The growth methods are reviewed in [9]. The shell is fragmenting under annealing into islands with sizes proportional to its initial thickness, and the diameters of the CNTs depend on the size and microstructure of the islands. The alignment of nanotubes, normal to the substrate surface, was found to be strongly depended on the electric field nearby the substrate surface in the case of PECVD or to be controlled by the configuration of the lateral surfaces of the porous on nanoporous substrates in the case of CVD.

Alternatively, a catalyst can be injected into the deposition volume directly during the deposition process in the form of the catalytically active material (injected catalyst) [10]. The CVD method using continuous injection of catalysts (CIC-CVD) is a very efficient and popular way to produce a large area of vertically aligned CNTs (VANTs) with uniform height in a millimeter range and with a negligible amount of amorphous carbon [11–13]. Here we describe in a concise way the CIC-CVD method and results of structural and compositional characterization of large arrays of VANTs. We investigate the changes of the catalyst structure during the CNT growth and continuous supply of the catalyst particles, and its interaction with the CNT. We show that catalyst particles agglomerate either in the CNT channel or inside the CNT wall, or at the CNT side, forming catalyst nanocrystals. A variety of the structures of α-Fe(C), γ-Fe(C) and orthorhombic Fe_3C phases is observed. A monoclinic distortion of the cubic lattice of the γ-Fe(C) is identified with orts $c > a = b$ and square base transformed into a rhombic one. The symmetry distortion is referred to the uniaxial symmetry of the encapsulating tube. A

[1] The article is published in the original.

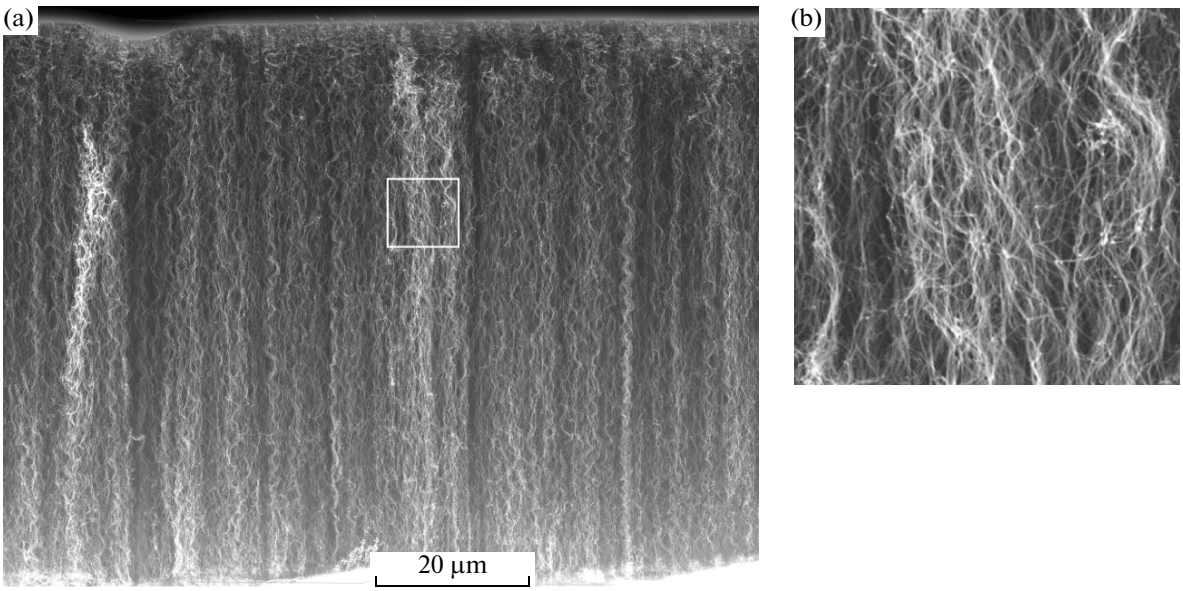

Fig. 1. A typical cross-sectional SEM image of VANTs array (a); zoomed in fragment of the VANT array, squared in Fig. a (b).

coherency in atomic arrangement at the interface between Fe particle and inner shell of carbon tube, as well as coherency in atomic arrangement of neighboring graphene shells of the CNT wall, is analyzed and discussed.

EXPERIMENTAL METHODS

The arrays of VANTs were obtained by pyrolytic gaseous deposition using continuous injection of catalyst, similar to the method previously reported in a number of papers [10–13]. In this method [14], a liquid solution of ferrocene in cyclohexane, served as an active media, was supplied into an CIC-CVD reactor—quartz tube (length of 100 cm and diameter of 2.5 cm) placed in an automatic temperature controlled oven. Rates of supply of support gases (N_2 and H_2) were controlled automatically and independently. The liquid solution evaporated in a low temperature zone (~200°C) and a flow of the support gas saturated with the active vapor components in a high temperature zone at the set temperature in a range of 750–950°C (typically 850°C) where active components decomposed. The ferrocene, or bis-cyclopentadienyl iron C5H5–Fe–C5H5, decomposed. Iron condensed on a substrate and nanoislands as catalyst particles were formed. The cyclohexane pyrolyzed to carbon forming a dense CNT forest on the catalyst shell. CNT growth conditions were optimized by changing support gas flow rates, the rate of the active solution ingress, the temperatures of the first (low) and second (high) zones.

Thus, uniform forest array up to of 15 × 100 mm^2 was obtained on a Si plate, as well as on many other substrate plates or textile materials. The length of the VANTs depended on growth conditions and it could reach 1 mm in an hour.

Structures of grown CNTs were investigated using field-emission-gun electron microscopes: scanning (SEM) TESCAN (Skobeltsyn Institute of Nuclear Physics, Moscow State University) and transmission (TEM) JEOL-2010 (Groningen University) ones. The composition was determined by X-ray microanalysis (spectrometer INCA Energy 250/X-max 80 attached to SEM TESCAN and Bruker QUANTAX microanalysis system in JEOL-2010).

For SEM studies, it was possible to investigate the cross-section of a sample chip. For TEM studies, a small piece of VANTs was chipped off the array. Then, CNTs were dispersed in an ethanol slush using a mortar and pestle, dissolved in a large volume of ethanol, dropped on a copper grid covered with holey carbon film, and dried in air. The CNTs laid over a carbon pore were examined in TEM.

STRUCTURAL CHARACTERIZATION BY TEM STUDY AND EDS ANALYSIS

A typical cross-sectional SEM image of 72 μm VANTs array is shown in Fig. 1. VANTs in the array are not straight but wavy and arranged in a vertical columns where CNTs contact with neighboring ones either directly or via entangled splits. The shape of CNTs obtained by CIC-CNT method differs from the shape of those obtained by pyrolytic gaseous deposition with predeposited catalyst where the CNTs are more entangled and randomly oriented, and by arc discharge deposition where CNTs are straight or slightly bended [15, 16]. The TEM image (Fig. 2) shows a couple of thick tubes with thin sprouts serving

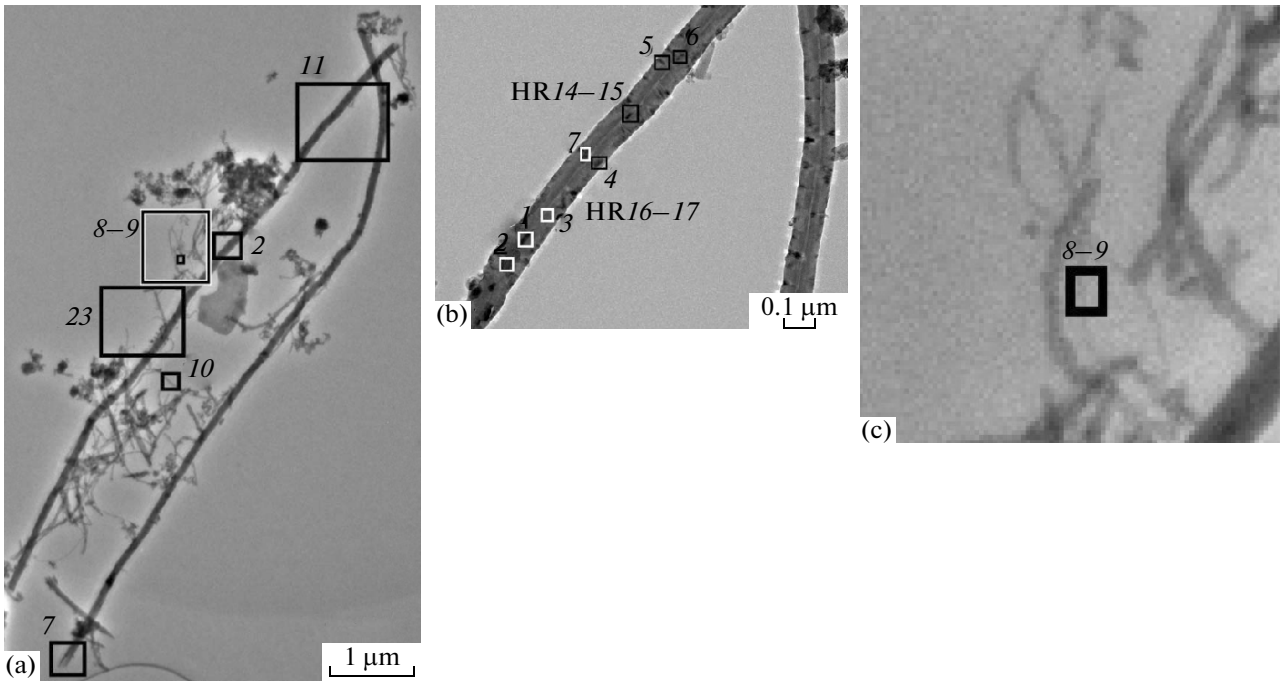

Fig. 2. Low magnification images of CNTs: (a) TEM image with numbered areas of the sample consisted of thick and thin MWNTs; (b) magnified fragment of the image squared and numbered as *11* in figure a showing areas with a dark contrast in the CNTs; (c) zoomed in fragment including a thin CNT and the region *8–9* squared in figure a. Some numbered positions are reproduced in the following figures as high resolution (HR) images or EDS spectra.

as intermediators binding VANTs in an array of columns. It provides a certain toughness of the array, strong enough to keep a unity during departing the array from the substrate, overcoming the adhesive force.

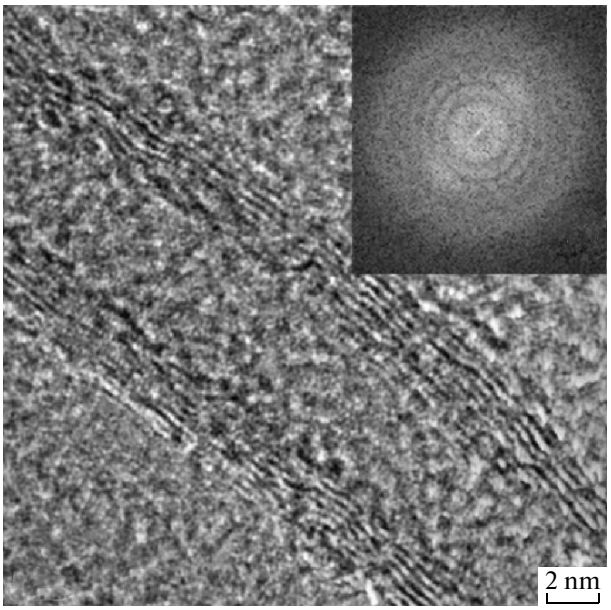

Fig. 3. HRTEM image of the fragment *8–9* marked in Figs. 2a, 2c and fast Fourier transform of the image (in the insert).

The walls of CNTs consist of multiple shells (multiwall nanotubes (MWNTs)). Diameter of the CNTs varies from 10 nm (thin CNTs) to 90 nm (thick ones). The inner diameter varies from ≈4 to ≈10 nm.

High resolution TEM (HRTEM) image (Fig. 3) shows a nanotube with seven shells. Capture areas are numbered by *8–9* in Fig. 2a, c where one of the thinnest tubes is shown. The fast Fourier transform (FFT) of the high resolution TEM image corresponds to a series of bright concentric rings (insert in Fig. 3). The second ring in the series contains two bright diffuse spots, corresponding reciprocal space vectors are oriented perpendicular to the CNTs walls. The distance between spots corresponds to the reciprocal wave number $k = 5.47/2$ nm^{-1} and to the intershell distance in the CNT wall $d_{is} \approx 2/5.47 = 0.366$ nm. This distance is longer than the distance between graphene shells in graphite (0.34 nm). The difference in the distances can be explained by a presence of isolated or clustered iron atoms inside the nanotube wall. The first ring and central reflections in the FFT pattern show no clear speckles corresponding to randomly distributed contrast fuzzed by instrumental uncertainties. The first ring probably corresponds to the periodicity of $2/4.0 = 0.5$ nm which, possibly, is a reflection from the porous amorphous carbon support film [17].

Figure 4 shows a HRTEM image of a thicker CNT wall. Bright spots in the FFT image (*1* in the insert) illustrate a good spatial periodicity of the graphene shells in the wall with the average distance between the

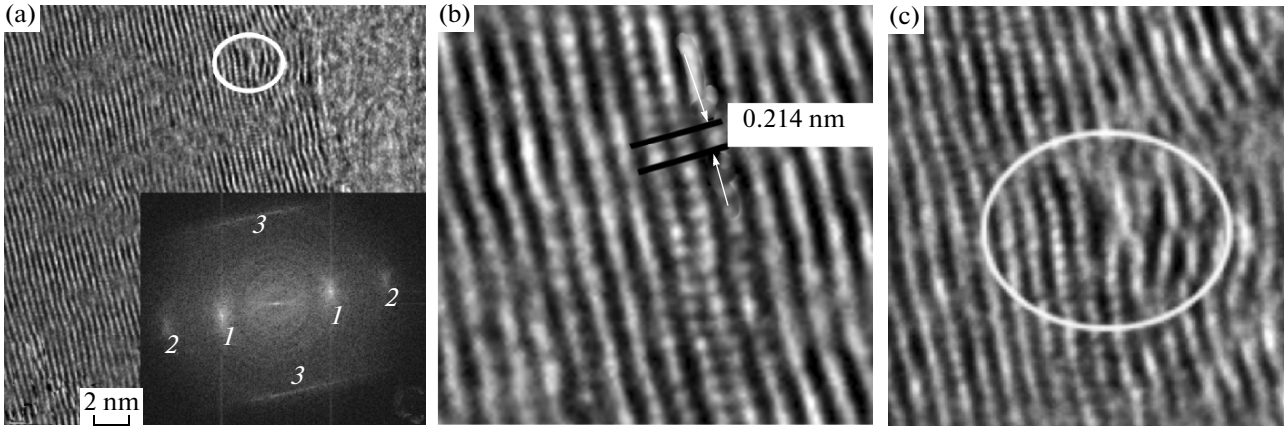

Fig. 4. HRTEM image of a fragment of a thick tube (a) and fast Fourier transform of the image (b); magnified image with a distinct discretization of the CNT shells in the center of the CNT (c); zoomed in image of the CNT shell split encircled in Fig. a (d).

shells $d_{1-1} = 2/5.841 = 0.342$ nm for inner two spots. The external two spots (*2*) are the second order reflections ($d_{2-2} = 2/11.821 = 0.169$ nm).

There are several features in the fast Fourier transform patterns (in the insert in Fig. 4) worth paying attention to. The straight vertical lines crossing the inner spots of CNT shells, evidently, are not related to any real structure, but rather to limitations of the FFT procedure. However, the two straight lines (*3*) parallel to the axis connecting graphene reflections and, hence, perpendicular to the orientation of the CNT shell fringes can be related to the inner periodical discreteness of the shells. This kind of streaking in the reciprocal space is called "relrod" in the TEM terminology and reflects a shape effect of the object, i.e. a small size of the object in certain direction(s). The intensity of electron beam diffracted in an idealized thin foil specimen with the dimensions of $N_a\mathbf{a}$, $N_b\mathbf{b}$, $N_c\mathbf{c}$ is written as

$$I = F^2[(\sin^2(\pi N_a\mathbf{K}\cdot\mathbf{a})/\sin(\pi\mathbf{K}\cdot\mathbf{a})] \times [(\sin^2(\pi N_b\mathbf{K}\cdot\mathbf{b})/\sin(\pi\mathbf{K}\cdot\mathbf{b})] \times [(\sin^2(\pi N_c\mathbf{K}\cdot\mathbf{c})/\sin(\pi\mathbf{K}\cdot\mathbf{c})], \quad (1)$$

where F is the structure factor, $\mathbf{K}$ is the change of the wave vector $\mathbf{k}$ due to the diffraction [18]. A large number of scattering atomic planes gives a sharp dot-like reflection, while a limited number of planes in one direction, for example, y direction perpendicular to the plane of the graphene shell, gives a spread of vector $\mathbf{K}$, according to the ratio [18]:

$$\mathbf{K}\cdot\mathbf{b} = C/(2N_b), \quad (2)$$

where C is an integer number. When the length of the streaks $2K$ is equal to 3.241 nm^{-1} we obtain $N_y b/C = 0.309$ nm which approximately corresponds to the nearest graphene plane distance in graphite for $C = 1$. A coherent arrangement of atoms in neighboring graphene shells can be concluded to be very restricted or, in other words, the coherency is rather weak on the average. Thus, there is no coherent chirality in the MWNT shells.

The distance 9.411 nm^{-1} between the streaks in the fast Fourier transform pattern (the insert in Fig. 4) gives the spacing within the x direction $d = 2/9.411 = 0.213$ nm which is in a good correspondence with direct estimates of the discreteness period from the HRTEM image of the CNT shells (Fig. 4b).

The CNT shells fringes are not arranged ideally. They show distortions like shell bending or like a kind of edge dislocations (encircled in Figs. 4a, 4c). Elongated pieces of a black contrast between the shells nearby a dislocation indicate that dislocated areas may be caused by precipitation of subnano-sized catalyst particles.

Dark contrast areas are also visible in the large scale images (Fig. 2b). This contrast is visible in the center as well as at the periphery of the tube. Some areas are elongated rod-like objects aligned parallel to the tube axis. The other ones have the triangular shape and are peaked from the periphery to the channel center. Some of these contrast areas were revealed using energy-dispersive spectroscopy (EDS) due to the presence of Fe-containing particles.

The EDS spectra are shown in Figs. 5a–5e in different positions along the CNT marked in Fig. 2b and enlarged in the inserts. The spectrum in Fig. 5a measured in a clean CNT area (*3* in Fig. 2b and in the insert) is composed predominantly of C- and Cu-lines. The latter ones are due to the Cu-based grid and the sample holder. There are no traces of iron in the spectrum (Fig. 5a). In contrast, strong Fe-lines in the spectrum (Fig. 5b) appear with a dark elongated particle in the CNT channel when the beam is moved to the position *1* (Fig. 2b and in the insert). Thus, we conclude that this is Fe-containing particle. We call these

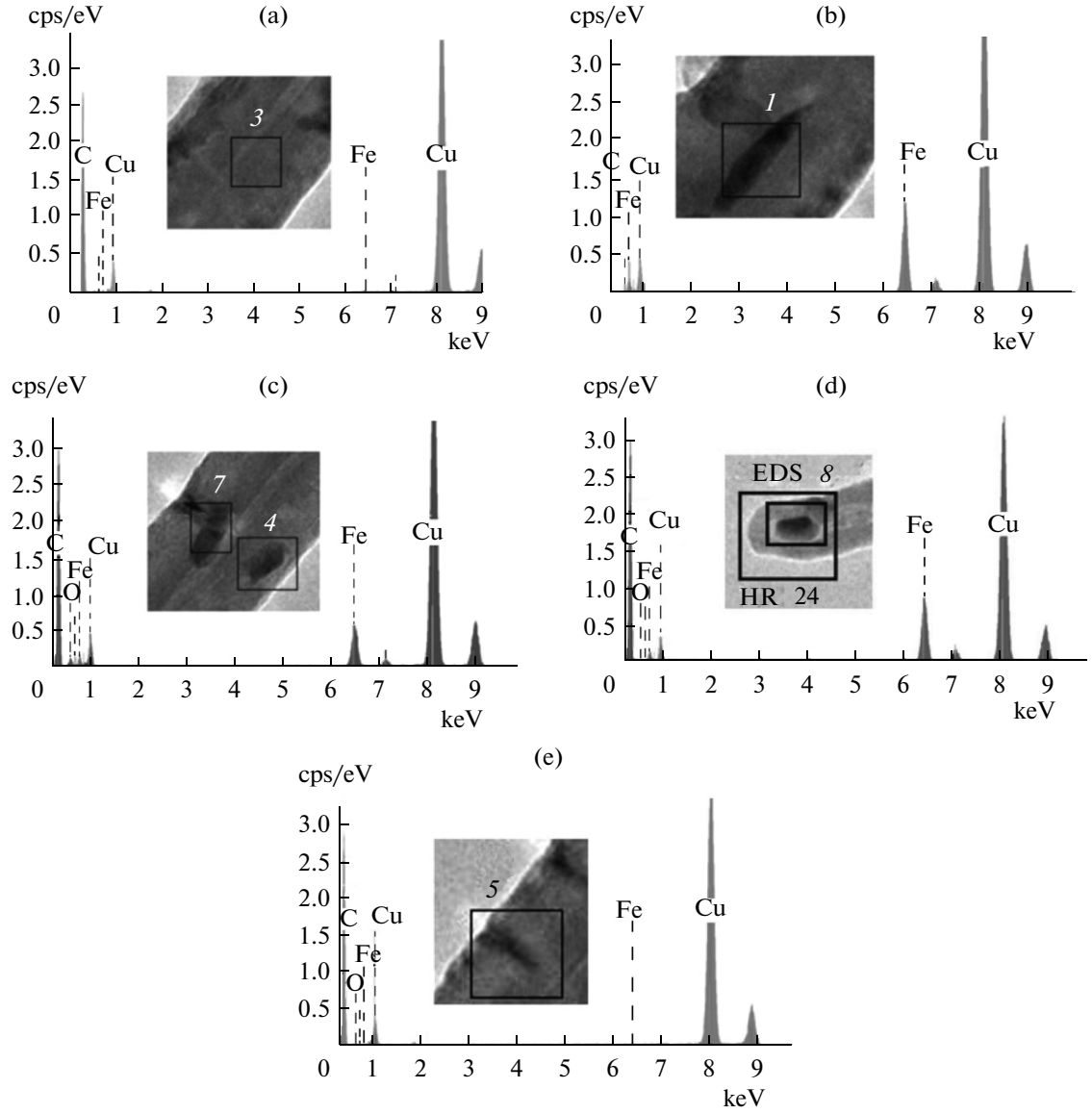

Fig. 5. EDS spectra of different CNT areas: (a) clean CNT; (b) Fe and CNT channel; (c) Fe and CNT wall; (d) Fe in thin CNT channel close to the CNT tip; (e) triangular contrast spot and CNT periphery.

objects Fe particles but EDS method cannot define whether this particle is a pure Fe or a Fe_xC carbide. This problem can be solved using HRTEM.

The spectrum in Fig. 5c was measured in the position *7* (Fig. 2b and in the insert). That is the area where Fe particle is slightly moved from the CNT channel. The spectrum shows, besides the Fe-lines, also the oxygen *K*-line indicating that Fe particle is at least partially oxidized, providing evidence that the Fe particles can grow not only at the centers of the channel but also at the periphery of the CNT.

Figure 5d demonstrates that oxygen is absent in the Fe particle at the tip of a thin CNT. The spectrum in the Fig. 5e was measured at the CNT periphery in the dark contrast area (5 in the insert). Since there is no indication of presence of any elements besides carbon and copper according to EDS spectra the dark contrast area in the image is concluded to be due to structure defects and not due to presence of a heavy element in this area of CNT.

Fe PARTICLES

HRTEM observations of Fe particles provide important information about their structures. The HRTEM dark contrast area image in the carbon nanotube center is shown in Fig. 6a. The position of the contrasting particle numbered as 15 in the list of inspections is illustrated in the lower insert in Fig. 6a. The fast Fourier transform of the image is shown in the upper insert in Fig. 6a. The FFT pattern shows that, as in the previous cases, there are reflections correspond-

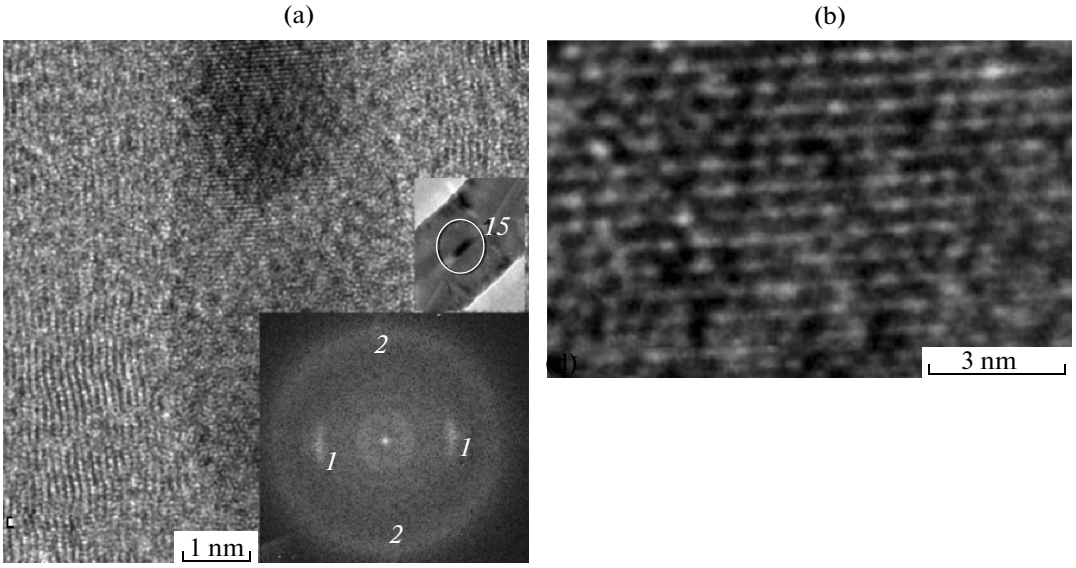

Fig. 6. HRTEM image of Fe particle in the CNT channel (a), low magnification image showing location of the Fe particle (in the upper insert), fast Fourier transform pattern of the image (in the lower insert); HRTEM image of a fragment of the Fe particle (b).

ing to the CNT walls with spacing $d_{1-1} = 2/5.791 = 0.345$ nm which is in a good correspondence with the spacing in graphene planes of crystalline graphite. In addition, there is an external diffused ring with two weak spots in the fast Fourier transform pattern which correspond to the planes oriented almost perpendicular to the CNT wall fringes. The particle interplanar spacing $d_{2-2} = 2/9.8 = 0.204 \pm 0.003$ nm is in correspondence with directly counted spacing between planes visible in the high resolution dark contrast area image and in the boundary of the dark contrast area of the particle. We note that this distance between planes corresponds approximately to the spacing between (110) planes of body-centered cubic (BCC) α-Fe (0.2027 nm) or $(1\bar{1}1)$ planes of face-centered cubic (FCC) γ-Fe (0.2067 nm), or (220) and $(\bar{2}\,20)$ places of orthorhombic Fe_3C (0.2031 nm). There is also discreteness along these plane fringes with closest distance 0.21 nm between contrast bright spots. The image does not provide more detailed identification of the particle.

Figure 7a represents a HRTEM image of the area numbered as 16 in the lower insert. The Fe particle is located at the periphery of the multiple-wall CNT. Two brightest spots in the FFT pattern (*1* in the upper insert in Fig. 7a) correspond to CNT shell fringes separated by the distance $d = 2/5.291 = 0.378$ nm. The significant deviation from 0.34 nm graphite spacing is evidently due to influence of the catalyst particle which is visualized in the FFT pattern as a crystallite (upper insert in Fig. 7a). The analysis of reflections *2*, *3* and *4* in the pattern allows identifying the image as Fe_3C cementite with zone axis [131]. The corresponding simulated reciprocal lattice is shown in Fig. 7b. It is also important to note the CNT fringes overlap Fe_3C fringes (Fig. 7a) validating the incorporation of the cementite type crystal into the CNT wall.

Another case of catalyst image is illustrated in Fig. 8a where the Fe particle is shown fully encapsulated in the channel at the CNT end. The fast Fourier transform pattern reveals three rings and four dot-like reflections. The regular graphene fringes surrounding the particle give almost uniform ring *1*, the more intensive and corresponding to the intershell spacing in the CNT equal to $d_{1-1} = 0.375$ nm. This spacing is close to that described above for Fe particle. The dot-like reflections *2–5* encircled for easy recognition are located at distances corresponding to the interplanar spacings of 0.179, 0.227, 0.216, and 0.142 nm respectively. The spacings together with overall pattern configuration lead to identification of the encapsulated Fe particle (Fig. 8a) as a distorted γ-Fe(C) crystallite with zone axis $\mathbf{B} = [011]$ (the insert in Fig. 8a) and the lattice parameter $a = 0.3573 + 0.0033C = 0.358$ nm where C is the carbon concentration, $C \approx 0.3$ at %. The spots *2*, *3*, *4*, and *5* correspond to (200), $(1\bar{1}1)$, $(11\bar{1})$, and $(02\bar{2})$ planes respectively. The distances between $(1\bar{1}1)$, $(11\bar{1})$ and $(02\bar{2})$ planes are longer by 9.8, 4.5 and 12.2 percents than the corresponding distances in γ-Fe. In other words, in addition to general lattice expansion, the difference in the distances between two first reflections indicates the distortion of the cubic lattice. The analysis shows (see Appendix) that this distortion can be represented as a small transformation of the FCC lattice into a monoclinic lattice with the orts $c > a = b$ and rhombic base. Such deformation probably indicates the existence of the intermediate phase on the way to orthorhombic Fe_3C reported in [13].

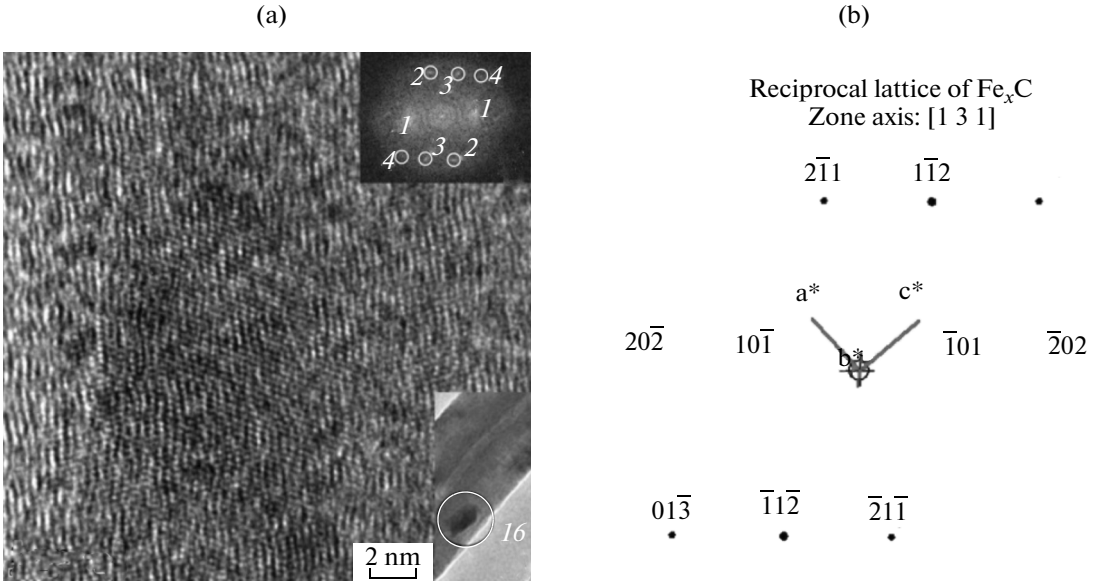

Fig. 7. HRTEM image of Fe particle at the periphery of the CNT (a), location of Fe particle (area 16) (in the lower insert); fast Fourier transform of the image (in the upper insert); simulated reciprocal pattern for [131] pole of orthorhombic Fe_xC phase ($x = 3$) (b).

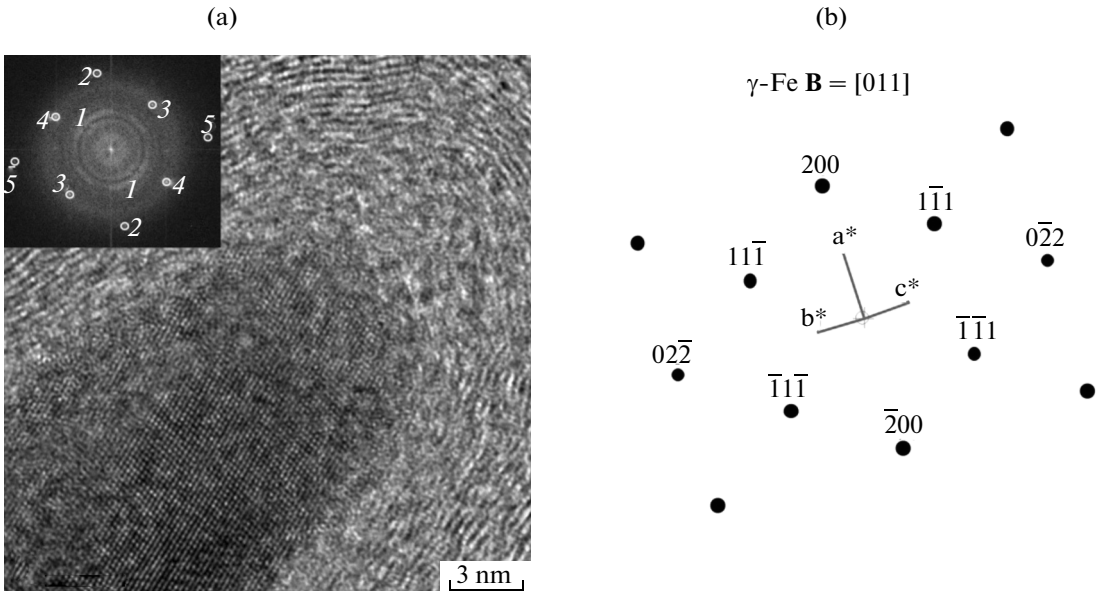

Fig. 8. HRTEM image of Fe particle at the end of the CNT channel (a) and fast Fourier transform pattern with encircled reflections (in the insert); simulated reciprocal pattern for zone axis [011] of FCC γ-Fe(C) particle (b).

The Fig. 9a shows another Fe particle in the CNT channel. In contrast to the previous images, this one demonstrates clearly defined facets of Fe particle. Zoomed in images of different sides of the particle/CNT interfaces are displayed in Figs. 9b–9e. The facets are outlined in Fig. 10a, the fast Fourier transform of the image shown in Fig. 9a is given in Fig. 10b. According to the FFT pattern, the spacing between the CNT shells $d_{1-1} = 2/5.811 = 0.344$ nm which corresponds nicely to the graphite interplanar distance (spots *2* are just the second order reflections, $d_{2-2} = 0.172$ nm). The fast Fourier transform of Fe particle image is represented by spots *3* and the plane fringes spaced by 0.178 nm which is close to the spacing between (200) planes in γ-Fe. The facet *A* is aligned parallel to the CNT fringes. The facets marked as *B* and *D* (Fig. 9a), more diffused than other facets, are predominantly aligned parallel to the (200) plane

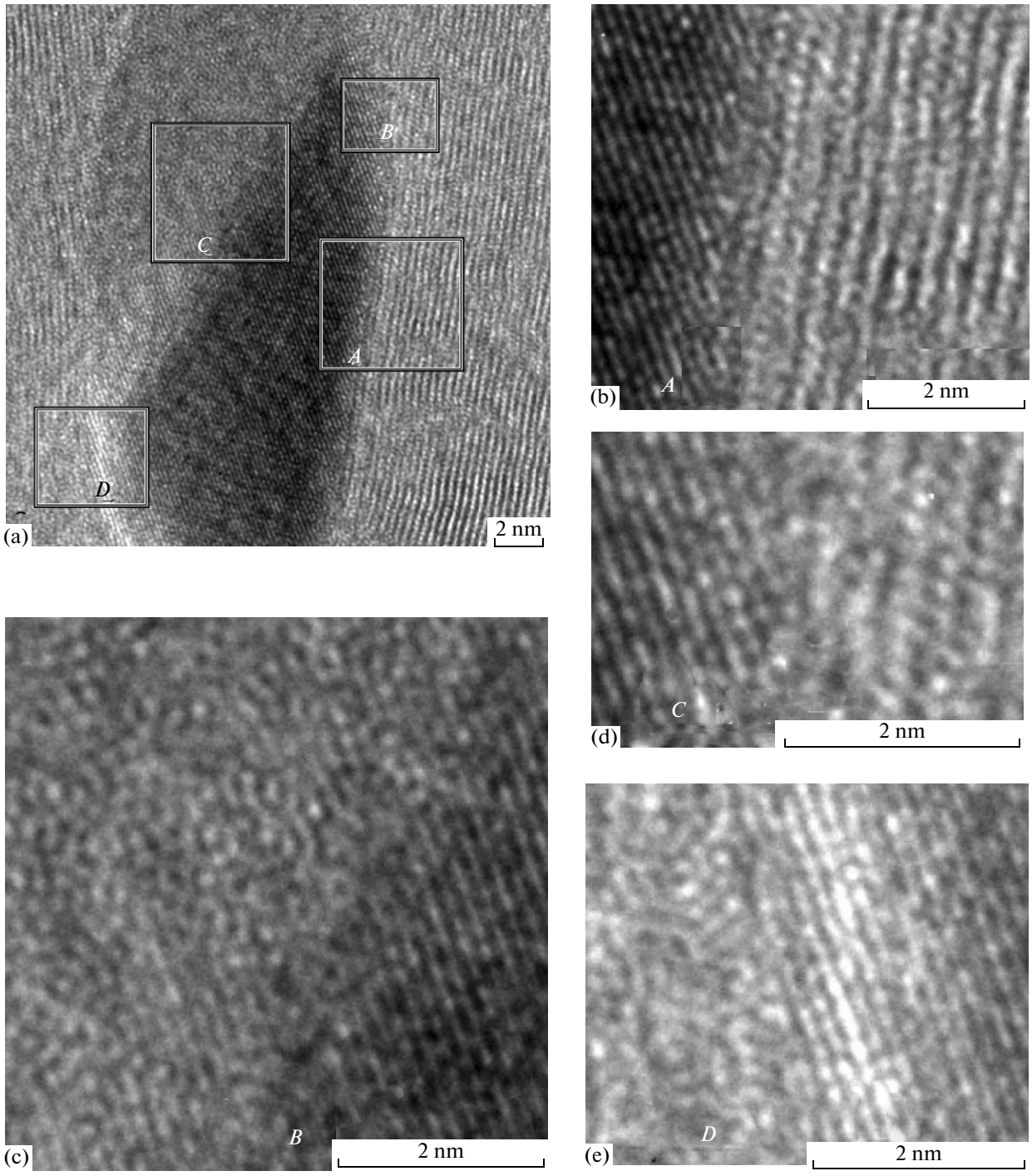

Fig. 9. High resolution image of *A*, *B*, *C* and *D* areas (a) zoomed in: *A* (b); *B* (c); *C* (d); *D* (e) respectively.

while the facet *C* makes the angle $\alpha = 55° \pm 1°$ with the facet *B* which is in a good agreement with the angle 54.74° between (200) and (111) planes in a FCC lattice. The angle between *A* and *B* facets is about $\beta = 150°–153°$. The 154.76° angle between $(\bar{2}00)$ and $(3\bar{1}\bar{1})$ planes is close to this value. This identification is not unambiguous since the facet *A* can be visually limited, more by CNT walls than by mutual orientation of crystallographic planes in Fe particle. If it is so, the pole of the image of Fe particle is the [011] pole, the same as for the particle in Fig. 8a.

A careful inspection of the boundaries from *A* to *D* between the Fe particle and CNT walls does not give an evidence for coherency of the interface. In most cases, there is a strong distortion of the interface layer

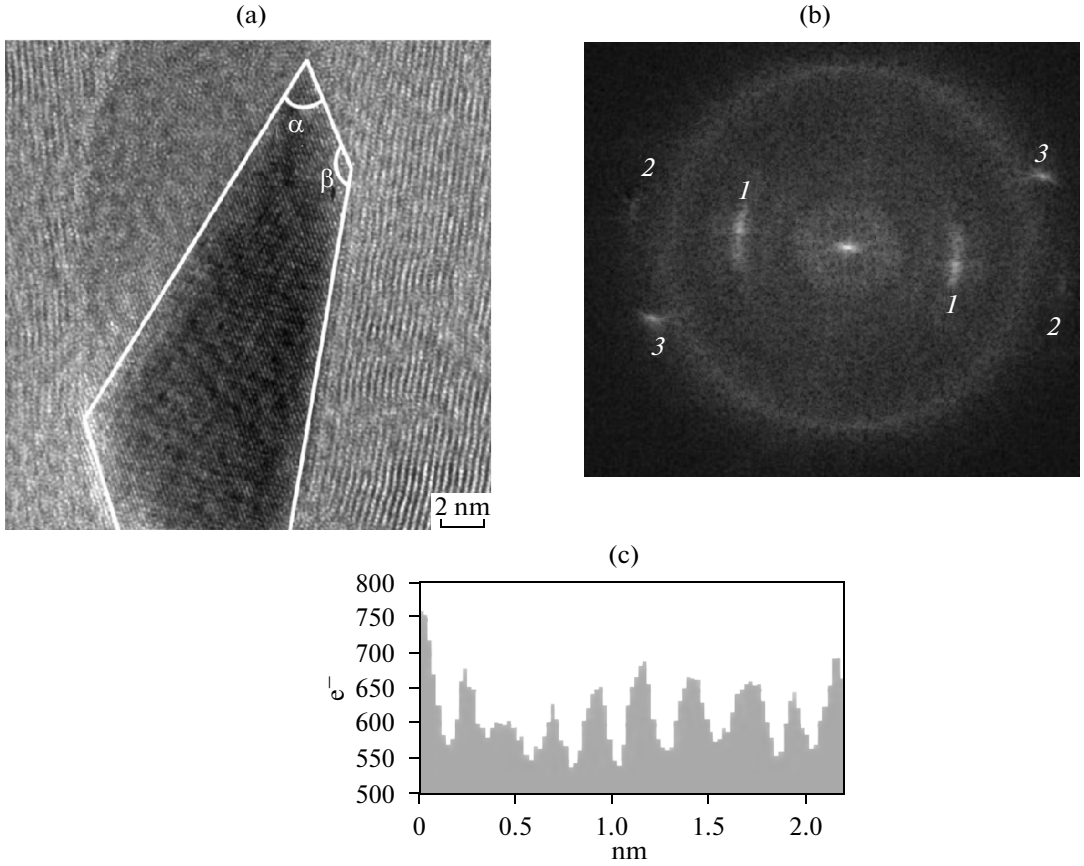

Fig. 10. The same image as in Fig. 9a but with delineated facets (a); fast Fourier transform pattern of the image (b); typical contrast modulation along the CNT shell fringe (c).

which has the same thickness as couple of CNT shells. A primary estimation of the misfit distance between the (200) plane cut by the facet *A* (0.179/cos(151.5° – 90°) = 0.375 nm) and a typical discrete contrast along CNT wall ≈0.24 nm, as can be estimated from Fig. 10c, gives a too large misfit value ((0.375 – 0.24)/0.24 = 0.56, or (0.375 – 0.24)/0.375 = 0.36, or (0.375 – 2 × 0.24)/0.375 = –0.28). This can be considered as an explanation of the structural disorder at the interface and indication of a complicated mechanism of CNT growth where the role of Fe catalyst is still unclarified.

DISCUSSION

A large area growth of aligned CNTs is a very prospective trend if the height, packing density, aspect ratio and other important characteristics of the individual CNTs are under control during the growth. The deep knowledge of the growth mechanisms and related processes is required. In the specific CIC-CVD method, the role and behavior of iron continuously supplied together with ferrocene during the growth are of great importance. The structural correspondence of CNTs and iron is possibly an important clue for solving the problem.

It was shown that the major part of the CNTs had a thick multishell construction containing sprout-type thin tubes. Iron nanocrystals were observed in the CNT channel as well as iron embedded in the CNT wall. There were also areas in the CNT walls where Fe was not detected. This allowed suggesting the clustering of nanocrystalline Fe particles caused by diffusion of atomic Fe into a particle of a larger size and by iron deficiency in the surrounding CNT. The diffusing Fe atoms can move along the channel sliding over inner surface of the tube or slipping between the wall shells and then penetrate through the shells. The driving force for such motion is the stress in the CNT due to presence of Fe either in substitutional or interstitional position within the shell or in intershell position. These stresses were found by expansion of intershell spacing and its restoration to the value of interplanar distance in graphite in areas surrounding the Fe clusters. The observation of the cluster within the CNT wall, as depicted in Fig. 7, was the most surprising. Evidently, the cluster was formed simultaneously with the CNT shells.

Summary of the analysis of the images in Fig. 8

Reflection	(*hkl*)	d_i	$\underline{d}_i$	$\Delta d_i/d_i$
2	(200)	0.179	0.179	0
3	$(1\bar{1}1)$	0.2067	0.227	0.098
4	$(11\bar{1})$	0.2067	0.216	0.045
5	$(02\bar{2})$	0.1266	0.142	0.122

d_i—interplanar distances in the original lattice; $\underline{d}_i$—the same in the distorted one.

The Fe particles were found in the form of γ-Fe with increased lattice parameter and monoclinic lattice distortion, as well as in the form of orthorhombic $Fe_\delta C$ with $\delta \approx 3$ and α-Fe(C) phase. The atomic and subnano-sized clusters were assumed to be dissolved in the CNT wall increasing the intershell spacing. A similar set of α-Fe, γ-Fe, and Fe-carbide phases was found in [19]. The cementite Fe_3C phase with [131] zone axis inside the CNT channel was identified previously in [13] and encapsulated in carbon nanocapsules [20]. The complete set of the α-Fe, γ-Fe and Fe_3C phases was reported in [21]. Our data are quite different from previous studies. We showed that at least some Fe nanoparticles in γ-Fe phase had increased lattice parameter due to the presence of dissolved carbon. There was a γ-phase with a cubic lattice transformed into monoclinic one. The monoclinic type lattice had $c > a = b$ orts and square base distorted to the rhombic one. The distortion can be explained by uniaxial stress anisotropy induced by CNT and by presence of carbon in the lattice which occupies the interstitial positions. The restriction imposed by CNT walls leads to a radial compression of Fe crystals in the channel while the longitudinal expansion of nanocrystals is almost free.

Simple estimates of the misfit between iron and CNT lattice leaves no arguments that Fe/CNT interface can be structurally coherent. Instead, one can observe a certain disorder within couple of interface shells. This observation does not exclude the influence of Fe catalyst on the CNT structure formation because the final image is "frozen" at room temperature, while the CNT grows in a dynamic mode with smaller size particles at 850°C. At this temperature Fe particle can be mechanically softer and can easily adapt for CNT lattice. Cooling down leads to formation of the edge-like and other type dislocation not only at the interface as shown by HRTEM images but also in the bulk wall structure (Figs. 4a, 4c).

The discrete contrast of the MWNT shell fringes appears in many HRTEM images though the contrast modulations in most parts of the images are smoothened by lack of spatial resolution. We assume that these contrast modulations reflect the atomic arrangement in the graphene shells. The atomic resolution of multi-wall carbon nanotubes was reported earlier in [22, 23]. The 0.213 nm periodicity in the contrast modulation is in exact correspondence with projection of **a**-ort on the CNT axis ⟨001⟩ ($0.246\cos 30° = 0.213$ nm). Such a precise correspondence is even excessive but can be considered as an indication of the armchair type of the chirality of this particular CNT shell. There is no definite coherency in crystallographic atomic arrangement of the neighboring shells in the MWNT. Our observation is in agreement with conclusion of [24] where the structural correlation between two adjacent graphitic shells in double-wall carbon nanotubes was systematically examined by using electron diffraction and correlation of chiralities between the inner and external tubes was found to be random. However, this conclusion is in contrast with single-chirality in multi-walled carbon nanotubes reported in [25, 26]. The latter observation is surprising since it contradicts to simple geometrical arguments lead to a conclusion that in general the MWNT should consist of individual shells of independent chirality, precluding any crystallographic matching of neighboring graphene-like shells [26]. The authors refer to the observed single chirality as a special case connected with nitrogen doping of MWNT during the growth. It should be noted that in fact the lack of the coherency does not impede the shells in the wall to have the same chirality. The coherency may be broken by a random

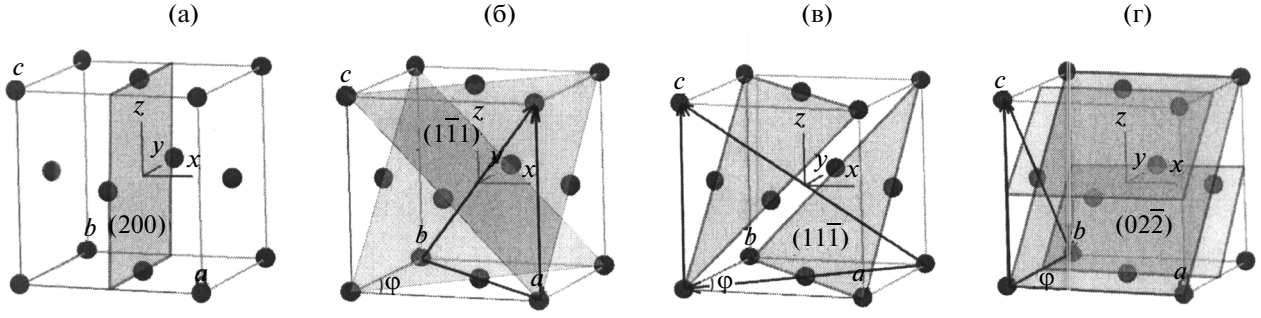

Fig. 11. An illustration of the arrangement of the main planes in γ-Fe phase.

translation along and random rotation around the tube axis.

Several mechanisms of catalytically assisted CNT growth with pre-deposited catalyst [27] were discussed. Traditionally, it is assumed that in the case of the pre-deposited catalyst the growth occurs either via the base-growth mechanism when new C atoms released from oversaturated catalyst build in the bottom of the CNT lattice, or via tip-growth mechanism. The nucleating nanotube chips a tiny flake of catalyst, lifts it at the top of CNT, and is replenished by atomic carbon from this particle which serves an intermediator in the growing process.

In the CIC-CVD process, carbon atoms can be deposited on any open surface. Then, either this particle can be covered by carbon shell from the pyrolyzed carbonaceous gas or can move around until it segregates into a cluster (liquid or solid) with a size sufficient to function as a catalyst to supply the atomic carbon for CNT construction. Small clusters on the lateral surface of the CNT can nucleate new sprout CNTs orientated in different ways (Fig. 2a).

CONCLUSIONS

A detailed study of vertically aligned multi-walled CNTs was performed and the following conclusions can be drawn.

A large array of multi CNTs can be obtained using the method of continuous supply of iron-catalyst during the CNTs growth.

The spacing between the shells in the MWNTs was found to be enlarged due to presence of atomic or crystallized Fe particles.

The catalytic iron incorporates into CNT in the form of atoms and nanocrystallites.

The Fe-containing crystallites were observed as FCC γ-Fe(C), BCC α-Fe(C) and orthorhombic Fe_3C phases which were located in the CNT channel, in the CNT walls, and on the lateral surface of CNTs.

The cubic symmetry of the FCC γ-Fe(C) phase was observed to transform to monoclinic type phase with the orts $c > a = b$ and small distortion of square base plane of the lattice to the rhombic one.

No coherency between Fe particle and CNT at the interface was found.

No coherency in the atomic arrangement of neighboring graphene shells or in the chirality of the CNT walls was observed.

The help of Mr. Akimov N.B. and Dr. Makunin A.V. on different stages of the work was highly acknowledged. The work was supported by Russian Fond of Basic Research (grant nos. 14-02-01230 and 14-02-31147 mol_a).

APPENDIX

The results of analysis of images represented in Fig. 8 are summarized in the table. The interplanar spacings d_i in the third column are for virgin FCC lattice with $a = 0.358$ nm, while $\underline{d}_i$ in the fourth column are measured values for distorted FCC lattice. The orientations of the planes in the lattice are shown in Fig. 11.

A simplest distortion which could describe the increase in spacing between $(02\bar{2})$ planes $\Delta d_5/d_5 > 0$ is an elongation of the **c**-ort, i.e. $\underline{c} = a + \Delta c$. In this case, assuming the distortion to be small $\Delta c/a \ll 1$,

$$\begin{aligned}\Delta d_5/d_5 &= \{[1 + (1 + \Delta c/a)]/2\}^{1/2} - 1 \\ &\approx \Delta c/(2a) = 0.122.\end{aligned} \quad (A.1)$$

It gives $\Delta c/a \approx 0.244$.

The inequality $\Delta d_3/d_3 \neq \Delta d_4/d_4$ can be explained by the rhombic distortion of the square {001} base planes, i.e. $\underline{a} = \underline{b} = a$, but the angle between unit vectors $\underline{\mathbf{a}}$ and $\underline{\mathbf{b}}$ is not right, $\varphi \neq \pi/2$ (monoclinic crystal). In this case, for $(1\bar{1}1)$ planes:

$$\begin{aligned}&\Delta d_3/d_3 \\ &= \{[\underline{a}^2 + \underline{b}^2 - 2\underline{a}\underline{b}\cos\varphi + \underline{c}^2]/3a^2\}^{1/2} - 1 \\ &\approx \{1 - 2\cos\varphi/3 + (2/3)(\Delta c/a)\}^{1/2} - 1.\end{aligned} \quad (A.2)$$

Assuming the distortion to be small, i.e. $\varphi = \pi/2 - \alpha$ with $\alpha \ll \pi/2$ we obtain:

$$\Delta d_3/d_3 \approx 1 + \alpha/3 + (\Delta c/a)/3 - 1. \quad (A.3)$$

For $\Delta d_3/d_3 = 0.098$ and $\Delta c/a = 0.244$, we estimate $\alpha \approx 0.05$ (≈2.9°).

Similarly to $(11\bar{1})$ planes we obtain:

$$\Delta d_4/d_4 \approx 1 - \alpha/3 + (\Delta c/a)/3 - 1. \quad (A.4)$$

Using the values of $\alpha = 0.05$ and $\Delta c/a = 0.244$ we obtain $\Delta d_4/d_4 \approx 0.065$ which is slightly larger than the experimental 0.045 value. However, taking into account the uncertainties in the experimental values we conclude that this estimation validates the Fe particle (Fig. 8) as a distorted FCC γ-Fe(C) nanocrystallite.

REFERENCES

1. W. Z. Li, S. S. Xie, L. X. Qian, B. H. Chang, B. S. Zou, W. Y. Zhou, R. A. Zhao, and G. Wang, Science **274**, 1701 (1996).
2. S. Fan, M. G. Chapline, N. R. Franklin, T. W. Tombler, A. M. Cassell, and H. Dai, Science **283**, 512 (1999). doi: 10.1126/science.283.5401.512
3. X.-Z. Ding, L. Huang, X. T. Zeng, S. P. Lau, B. K. Tay, W. Y. Cheung, and S. P. Wong, Carbon **42**, 3003 (2004).

4. Z. F. Ren, Z. P. Huang, J. W. Xu, J. H. Wang, P. Bush, M. P. Siegal, and P. N. Provencio, Science **282**, 1105 (1998).
5. Z. P. Huang, J. W. Xu, Z. F. Ren, J. H. Wang, M. P. Siegal, and P. N. Provencio, Appl. Phys. Lett. **73**, 3845 (1998).
6. C. Bower, W. Zhu, S. Jin, and O. Zhou, Appl. Phys. Lett. **77**, 830 (2000).
7. M. Chhowalla, K. B. K. Teo, C. Ducati, N. L. Rupesinghe, G. A. J. Amaratunga, A. C. Ferrari, D. Roy, J. Robertson, and W. I. Milne, J. Appl. Phys. **90**, 5308 (2001).
8. B. Vigolo, C. S. Cojocaru, J. Faerber, J. Arabski, L. Gangloff, P. Legagneux, H. Lezec, and F. le Normand, Nanotechnology **19**, 135601 (2008).
9. H. Chen, A. Roy, J.-B. Baek, L. Zhu, J. Qua, and L. Dai, Mater. Sci. Eng. R **70**, 63 (2010).
10. C. N. R. Rao, R. Sen, B. C. Satishkumar, and A. Govindaraj, Chem. Commun. **15**, 1525 (1998).
11. P. J. Cao, Y. S. Gu, H. W. Liu, F. Shen, Y. G. Wang, Q. F. Zhang, J. L. Wu, and H. J. Gao, J. Mater. Res. **18**, 1686 (2003).
12. C. Singh, M. S. P. Shaffer, and A. H. Windle, Carbon **41**, 359 (2003).
13. A. K. Schaper, H. Hou, A. Greiner, and F. Phillipp, J. Catal. **222**, 250 (2004).
14. N. G. Chechenin, P. N. Chernykh, E. A. Vorobyeva, and O. S. Timofeev, Appl. Surf. Sci. **275**, 217 (2013). http://dx.doi.org/10.1016/j.apsusc.2012.12.162
15. A. V. Makunin, K. E. Bachurin, E. A. Vorobyeva, A. A. Serdyukov, and N. G. Chechenin, Phys. Chem. Mater. Treatm. **4**, 66 (2011).
16. A. V. Makunin, N. G. Chechenin, A. A. Serdyukov, K. E. Bachurin, and E. A. Vorobyeva, Inorg. Mater.: Appl. Res. **2**, 252 (2011).
17. R. F. Klie, D. Ciuparu, L. Pfefferle, and Y. Zhu, Carbon **42**, 1953 (2004).
18. D. B. Williams and C. B. Carter, *Transmission Electron Microscopy* (Plenum, New York, 1996), Chap. 17.
19. A. Graff, T. Gemming, P. Simon, R. Kozhuharova, M. Ritschel, T. Mühl, I. Mönch, C. M. Schneider, and A. Leonhardt, Microsc. Microanal. **9** (S03), 180 (2003).
20. T. Kizuka, K. Miyazawa, and D. Matsuura, J. Nanotechnol. **2012**, 613746 (2012). doi:10.1155/2012/613746
21. D. Golberg, M. Mitome, Ch. Muller, C. Tang, A. Leonhardt, and Y. Bando, Acta Mater. **54**, 2567 (2006).
22. D. Golberg, Y. Bando, L. Bourgeois, and K. Kurashima, Carbon **37**, 1858 (1999).
23. M. Miki-Yoshida, J. L. Elechiguerra, W. Antúnez-Flores, A. Aguilar-Elguezabal, and M. José-Yacamán, Microsc. Microanal. **10** (S02), 370 (2004). doi: 10.1017/S1431927604886677
24. K. Hirahara, M. Kociak, S. Bandow, T. Nakahira, K. Itoh, Y. Saito, and S. Iijima, Phys. Rev. B **73**, 195420 (2006).
25. S. Friedrichs, A. H. Windle, K. Koziol, C. Ducati, and P. A. Midgley, Microsc. Microanal. **11** (S02), 1536 (2005). doi: 10.1017/S1431927605503519
26. K. Koziol, M. Shaffer, and A. H. Windle, Adv. Mater. **17**, 760 (2005).
27. M. Kumar, in *Carbon Nanotubes—Synthesis, Characterization, Applications*, Ed. by S. Yellampalli (Intech Europe, Rijeka, Croatia, 2011), Chap. 8, p. 147.